Velocity map imaging of the dynamics of the CH_3 + HCl → CH_4 + Cl reaction using a dual molecular beam method

Rebecca A. Rose, Stuart J. Greaves and Andrew J. Orr-Ewing*

School of Chemistry, University of Bristol, Cantock's Close, Bristol BS8 1TS, UK

06 January 2010

*Author for correspondence
e-mail: a.orr-ewing@bris.ac.uk
tel: +44 117 928 7672
fax: +44 117 925 0612

Abstract

The reactions CH_3 + HCl $\rightarrow$ CH_4 + Cl($^2P_{3/2}$) and CD_3 + HCl $\rightarrow$ CD_3H + Cl($^2P_{3/2}$) have been studied by photo-initiation (by CH_3I or CD_3I photolysis at 266 nm) in a dual molecular beam apparatus. Product Cl($^2P_{3/2}$) atoms were detected using resonance enhanced multi-photon ionisation and velocity map imaging, revealing product translational energy and angular scattering distributions in the centre-of-mass frame. Image analysis is complicated by the bimodal speed distribution of CH_3 (and CD_3) radicals formed in coincidence with I($^2P_{3/2}$) and I($^2P_{1/2}$) atoms from CH_3I (CD_3I) photodissociation, giving overlapping Newton diagrams with displaced centre of mass velocities. The relative reactivities to form Cl atoms are greater for the slower CH_3 speed group than the faster group by factors of ~1.5 for the reaction of CH_3 and ~2.5 for the reaction of CD_3, consistent with the greater propensity of the faster methyl radicals to undergo electronically adiabatic reactions to form Cl($^2P_{1/2}$). The average fraction of the available energy becoming product translational energy is $\langle f_t \rangle$ = 0.48 ± 0.05 and 0.50 ± 0.03 for reaction of the faster and slower sets of CH_3 radicals, respectively. The Cl atoms are deduced to be preferentially forward scattered with respect to the HCl reagents, but the angular distributions from the dual beam imaging experiments require correction for under-detection of forward scattered Cl products. A correction function is deduced from separate measurements on the Cl + C_2H_6 reaction, for which the outcomes can be compared with published differential cross sections from crossed molecular beam experiments. Monte Carlo simulations of the dual beam experimental method suggest that the source of the depletion is secondary collisions of the slowest moving reaction products (in the laboratory frame) with unreacted reagents or carrier gas in one of the molecular beams.

1. Introduction

The determination of product state resolved differential cross sections (DCSs) provides a unique insight into the dynamics of bimolecular chemical reactions [1]. Intuitively, the simplest method for measuring DCSs is to cross two molecular beams of reagents in space and measure reaction-product fluxes as a function of scattering angle. Experimentally, the measurement of state resolved DCSs in this way is challenging because of low signal levels, which are a consequence of small reaction cross sections and the need to resolve products flying into a small solid angle subtended by a (rotatable) detector. Dilution of the quantum-state resolved signals by formation of products in multiple quantum states is particularly pronounced for reactions involving polyatomic molecules because many product states may be populated. Multiplexing methods such as velocity map imaging (VMI) that detect flux into all scattering angles simultaneously are clearly advantageous, but it is only relatively recently that crossed-beam experiments in conjunction with VMI techniques and state-specific detection have been possible for polyatomic molecule reactions. Thus, only a few systems have been studied in this way, including reactions of Cl, F and O atoms with alkanes (most notably methane) [2-17] and the F atom reaction with silane [18]. Experimental strategies that have been developed to overcome the problem of low signal levels include single-beam co-expansion (commonly referred to as PHOTOLOC) and dual-beam techniques; both methods employ a photoinitiation step in which photodissociation of a precursor molecule AX starts the following reaction sequence:

$$AX + h\nu \rightarrow A + X \qquad (1)$$

$$A + BC \rightarrow AB + C \qquad (2)$$

In co-expansion experiments, both AX and BC molecular species are entrained within a single molecular beam, which has the advantage of producing much higher product number densities than experiments using crossed molecular beams. Zare and coworkers [19] and Brouard and coworkers [20] were instrumental in the development and application of these PHOTOLOC experiments, so-called because in the photoinitiated scheme, the product lab frame speed distribution P(v) can be related to the centre-of-mass (CM) frame angular scattering distribution (which is proportional to the DCS) by a simple law of cosines relationship Direct inversion of

the P(v) distribution to obtain the DCS only applies unambiguously for reactions where the undetected co-product (C in reaction (2)) is an atom formed with a single well-defined internal energy. In polyatomic reactions, multiple internal energy states of the radical or molecular co-product are usually populated and direct data inversion either requires the assumption that the internal energy is zero [21], or an average value is deduced from analysis that incorporates the lab frame anisotropy [22]. Any assumptions made about the internal energy will have an effect on the returned DCS, with the tendency to overestimate the sideways scattered component [23]. Alternative analysis procedures include fitting basis functions to the experimental data, such as in the Legendre moment (LM) method developed by Brouard and coworkers, which has the advantage of allowing for a distribution of internal energies of the co-product [23-25].

The method referred to here as dual-beam is a special case of a crossed-beam experiment. The technique was developed by Welge and coworkers to study isotopic variants of the $H+H_2$ hydrogen exchange reaction in combination with Rydberg tagging of the H atom products [26]. The experimental set-up used in the work reported here is described in detail below, but in summary consists of two parallel molecular beams, one containing the species AX and the other the co-reactant BC. Photodissociation of AX creates A atoms or radicals, some small proportion of which travels in the correct direction to intersect the second molecular beam in a configuration which is similar to a true crossed-beam experiment. The crossing of the two sets of reagents can, however, take place closer to the gas nozzles in higher density regions of the molecular beam. Variants of this technique have been used for high kinetic energy resolution studies of the $O(^1D)+H_2$ reaction by Yang and coworkers [27], and were first used in combination with ion imaging detection for the study of the $H+D_2$ reaction by Kitsopoulos *et al*. [28]. More recently, the dual-beam and VMI approach has been used to study O + alkane reactions [29], the H + CD_4 reaction [30] (albeit with a skimmer to select a velocity subset of the photolytically generated H atoms) and Cl + RH (RH = ethane, methanol dimethyl ether, and methyl halides) reactions [31-33]. In both dual- and crossed-beam experiments the reaction volume is, in general, large compared to the detection volume (defined by the focus of the probe laser beam) and careful checks are required to investigate possible biases introduced by velocity-dependent density-to-flux conversions. The transformation

from the lab to CM frame is greatly simplified for the dual beam arrangement compared to single-beam co-expansion experiments, and assumptions about the internal energy of the co-fragment are not generally required, allowing the full speed-dependent DCS to be determined.

The reaction between chlorine atoms and methane has become a benchmark for developing an understanding of the dynamics of reactions of polyatomic molecules; the reaction has proven to be well-suited for examination of the effects of collision energy, vibrational energy, vibrational mode excitation, and bond-selectivity for the abstracted atom, and the nonadiabatic reactivity of spin-orbit excited chlorine atoms. Pioneering studies by Zare and coworkers [34] were the first to show that excitation of vibrational modes of methane gives rise to an enhancement in reactivity compared to reaction of the vibrational ground state. Subsequent studies, with selective stretch excitation of single bonds, have confirmed these observations and shown that the stretch-excited bond breaks selectively, with the remaining methyl fragment acting as a spectator [35-39]. Recent, state-of-the-art experiments by Liu and coworkers using crossed molecular beams and VMI have shown that vibrational excitation is actually no better at enhancing reactivity than an equivalent amount of translational energy [9]. We sought information on the electronically adiabatic and non-adiabatic dynamics by taking a different approach in which we studied the reverse CH_3 (CD_3) + HCl → CH_4 (CD_3H) + Cl reaction [40,42,44], with CH_3 (CD_3) generated by the photolysis of CH_3I (CD_3I) at 266 nm. The Cl(^2P_J) atom products of reaction under single-beam co-expansion conditions were probed quantum-state specifically and we investigated the adiabatic and non-adiabatic pathways producing Cl($^2P_{3/2}$) and Cl*($^2P_{1/2}$), respectively. The results for reaction at a mean collision energy of 22.3 kJ mol^{-1} were analysed using both PHOTOLOC [19,20] and LM [23] analysis methods and showed forwards scattered DCSs with an average internal excitation of methane corresponding to a fraction that is ~0.40 of the total available energy. 15±2.4% branching into the nonadiabatic Cl* product was observed for the reaction of CH_3 radicals, compared to 20±3% for the reaction of CD_3, and there is evidence that Cl* formation is favoured for the fastest CH_3 (CD_3) fragments from the photodissociation step.

Despite the availability of different experimental techniques to measure DCSs for bimolecular reactions, there have been only a few studies which compare the

outcomes of measurements made using the different techniques. In this paper, we first describe the modifications to our experimental setup to enable measurements using the dual beam technique, and then present the first results from this configuration for the CH_3 (CD_3) + HCl reaction. We focus on the Cl($^2P_{3/2}$) (adiabatic) reaction products and compare our results to previous measurements made using single-beam co-expansion methods, and analysed using the PHOTOLOC and LM fitting methods.

2. Experimental

Experiments were carried out using a velocity map imaging spectrometer, shown in figure 1, which has been configured for DC slice imaging [41]. This experimental set-up has been used previously for single-beam co-expansion experiments and the main features have been described in detail elsewhere [22,44]. Here we focus on recent modifications to the gas entry and image acquisition components required for dual beam imaging.

The dual beam set-up is shown in the inset to figure 1 and consists of two pulsed valves (General Valve Series 9). The upper, "on-axis" valve is aligned along the axis of cylindrical symmetry through all the ion optics, the time-of-flight (TOF) region and the microchannel plate (MCP) detector. The lower, "off-axis" valve is vertically displaced downward by 17.4 mm but is parallel to the upper valve and the TOF direction. The off-axis valve is mounted onto a PTFE faceplate attached to the repeller electrode, and the on-axis pulsed valve can either be mounted on the repeller electrode or horizontally displaced by ~12 mm and the gas expansion skimmed, as depicted in the figure. Both gas expansions occurred through apertures in the repeller plate. As the skimmer is mounted directly onto the repeller plate it carries the same voltage and thus no ground field leaks through the aperture to disrupt the velocity mapping fields. For unskimmed expansions, the channel through this metal electrode opens to the main vacuum chamber via a 40° conical aperture with a base diameter of 0.8 mm. This design of orifice improves the collimation of the molecular expansions [45]. Pure CH_3I (Aldrich, 99.5%) or CD_3I (CK Gas, 98%, 99.5% of D atoms), with vapour pressures of 400 and 342 Torr, respectively, enters via the off-axis pulsed valve, and HCl (Aldrich, 99+%) diluted to 75% in Ar and with a backing pressure of

760 Torr is expanded through the on-axis valve. Masses greater than that of HCl^+ were not observed in the TOF mass spectrum, providing evidence that there was no significant clustering in this molecular beam.

The photolysis laser wavelength of 266 nm was generated from the fourth harmonic output of a Nd:YAG laser (Continuum Surelite II); the UV laser beam intersected the CH_3I (CD_3I) molecular beam at 90°. About 10 mJ $pulse^{-1}$ of the horizontally polarised 266 nm radiation was loosely focused into a stripe (parallel to the molecular beam axis) in the reaction chamber by a 25-cm focal length cylindrical lens to liberate methyl radicals from CH_3I (CD_3I). The photodissociations of CH_3I and CD_3I at 266 nm have been well characterised by prior experimental studies. The quantum yields for spin-orbit excited $I^*(^2P_{1/2})$ are 0.68 [46] and 0.81 [47], respectively with the remaining iodine atoms formed in the ground $I(^2P_{3/2})$ electronic state and both pathways predominantly parallel in character with $\beta \sim 2$. The large spin-orbit splitting of $I(^2P)$ atoms produces a bimodal speed distribution of CH_3 (or CD_3) and therefore a bimodal distribution of the collision energies in our experiments, as shown in fig. 1 of ref. [40]. Methyl radicals formed in conjunction with I* and I in the photodissociation step will henceforth be distinguished as "slow" and "fast", although it should be recognized that in both cases the radicals are moving with very high speeds. CH_3 and CD_3 are formed vibrationally excited from the photodissociation, with the excitation mainly confined to the umbrella (v_2) bending mode, and this excitation is much more substantial for the fast than the slow channel. The average internal excitation of the slower set of CH_3 fragments is 250 cm^{-1} and for fast CH_3 is 1530 cm^{-1}. Incorporating all these known outcomes of the photodissociation step, the average collision energies for the CH_3 + HCl reaction are 18.6 and 30.0 kcal mol^{-1} for reaction of the slow and fast CH_3 radicals respectively. CD_3 radicals are formed with a slightly higher average internal excitation of 460 cm^{-1} for the slow channel and 1575 cm^{-1} for the fast channel, and average collision energies for the CD_3 + HCl reaction are 17.3 and 28.1 kcal mol^{-1}.

Methyl radicals which travel in the correct (upwards) direction intersect the HCl molecular beam where they may react, and the $Cl(^2P_{3/2})$ products are probed by 2+1 resonance enhanced multiphoton ionisation (REMPI) via the $4p\ ^2D_{3/2}$-$3p\ ^2P_{3/2}$ two-photon transition at a wavelength of 235.366 nm. The probe laser radiation was

generated by frequency doubling in a β-barium borate (BBO) crystal the output of a dye laser (Lumonics HD500) pumped by the third harmonic of a Nd:YAG laser (Spectra Physics GCR 230-10). About 1 mJ pulse^{-1} of probe laser radiation was focused into the reaction chamber by a 25-cm focal length spherical lens. The probe beam was offset vertically from the photolysis laser by 17.4 mm so as to intersect the HCl molecular beam, with further displacement by ~4 mm in the TOF direction to compensate for molecular beam speeds. The probe laser was delayed with respect to the photolysis laser by ~6.5 μs to allow sufficient time for the methyl radicals to reach the HCl molecular beam. The Cl^+ ions created in the REMPI step were accelerated towards, and velocity mapped onto a position sensitive detector consisting of a pair of MCPs (Burle Electro-Optics) a P47 phosphor screen and a charge coupled device camera (La Vision, Image Compact QE).

The product velocity map images show a dependence on the time delay between the photolysis and probe lasers in agreement with the observation of Toomes and Kitsopoulos [31]; at shorter time delays, products with fast lab frame velocities dominate, whereas for longer delays products with slower lab frame velocities are more pronounced. Thus, images are accumulated by stepping in increments of 250 ns across time intervals up to ~6 μs from the time at which signal is first observed. To capture all product speeds, the probe laser frequency is stepped across the Doppler profile of the chlorine atom products in 0.02 cm^{-1} steps and an image is accumulated by adding data from all time steps for a single laser frequency, then moving to the next frequency step and repeating the sequence. A significant probe laser background signal is observed, primarily from the probe induced photodissociation of HCl and resonant detection of the Cl atom products; this strong probe-laser only signal appears at low lab velocities and saturated a part of the detector. We therefore placed a beam block in front of the detector to prevent signal detection in this region. Shot-to-shot background subtraction was carried out by operating the probe laser at 10 Hz and the photolysis laser at 5 Hz and subtracting the probe only signal from the two-colour signal. The time delay and laser frequency steps and background subtraction were automated using a custom written LabView program with accurate timings obtained via a pulse generator (Berkley Nucleonics Corp, BNC 555) and images were obtained using event counting software (DaVis, La Vision).

To check for systematic errors in the dual beam method, we performed experiments on the $Cl + C_2H_6 \rightarrow HCl + C_2H_5$ reaction, initiated by the photodissociation of Cl_2 at 355 nm, and compared our results from REMPI detection of HCl to the crossed-beam experiments of Suits and coworkers [3]. These experiments did not require use of the beam block described above. The translational energy distributions we observed are in good agreement with those from the crossed beam experiments, but are somewhat broadened, primarily as a result of a wider distribution of collision energies in our experiments. Figure 2 shows a representative image from our apparatus, and the CM frame angular scattering distribution derived from it. Comparison with the crossed-beam data demonstrates that we under-detect products that are scattered downward in the lab frame (in this case, backwards scattered products in the CM frame, whose velocities oppose the velocity of the centre of mass). This bias could not be eliminated by variation of the experimental parameters, and we therefore instead derived an angular correction factor for our experiment by dividing the angular distribution from the crossed-beam experiments by that obtained from our dual-beam measurements. This experimentally derived correction factor can be applied to the results of other reactive scattering experiments as a multiplicative factor which accounts for the observed systematic under-detection of the downwards (lab frame) scattered products. The validity and robustness of this correction procedure are tested in the data analysis presented later. Reasons for the need to introduce the angular correction factor were explored by extensive Monte Carlo (MC) simulations as described in the next section.

3. Monte Carlo simulation of the experiment

Further investigation of the observed depletion of products scattered downward in the lab frame was carried out by Monte Carlo simulation of the experiment. A similar approach was used previously by Murray *et al.* in studies of Cl + RH reactions [33], and by Suits and coworkers in investigations of O + RH reactions [29], both using the dual-beam technique. Simulations were performed for the $CH_3 + HCl \rightarrow CH_4 + Cl$ reaction, quantitatively incorporating many facets of the experiment including the experimental geometry, properties of the gas expansions, laser foci and intensity distributions, and laser time delays. Parameters of the reaction such as the speed distributions of the methyl radicals and the reaction energetics were also included.

Simulations were carried out using an input DCS (that the reactive events randomly sample) that was uniform in scattering angle, as shown by the blue line in the middle panel of figure 3. The possibility of different extents of disposal of available energy into product translation versus internal excitation was included by allowing the fraction of this energy in product translation, f_t, to take a range of values from 0.02 – 0.98, with an interval of 0.02. In the calculations, the full bimodal speed distribution of faster and slower CH_3 radicals (associated with I and I* co-fragments) was considered. The MC calculations were used to generate simulated velocity mapped images, and these simulated images were analysed to extract angular and speed distributions for comparison with the known starting conditions for the simulations to test for any systematic biases in the design of the experiment.

The combined results of the MC simulations, summed over all f_t values show an approximately uniform DCS for much of the angular range, but which peaks sharply in the forwards direction because of over-detection of slow lab-frame speed products. Here, we define the scattering direction as that of the Cl atoms with respect to the relative velocity of the HCl reagents in the CM frame: thus, for the experimental configuration in which the CH_3 radicals are moving close to vertically upwards in the lab, and the relative velocities of the HCl molecules are therefore vertically downwards, the forward scattered component of the Cl atom products appears at the bottom of the velocity mapped images. The sharp forwards scattered peak would arise in the region that is excluded by the beam block in our experiments, thus the experiment is expected to measure angular scattering probabilities in the range $-1 \leq \cos\theta \leq 0.75$ with only small angular bias. Figure 3 also shows the simulated f_t distributions derived from images, displayed alongside the input values (blue dots), with both fast and slow CH_3 channels demonstrating the same $P(f_t)$ behaviour. The calculated $P(f_t)$ distributions exclude the forwards scattering region that is experimentally removed by the beam block, to make the results more readily comparable to our experiments. The effect of a spread in product speeds, which is greatest at high f_t, combined with a lower detection efficiency for high f_t products result in the observed drop in $P(f_t)$ at high f_t for both channels.

The simulation outcomes indicate that little bias should be observed in the angular distributions, and a similar result is obtained for simulations of the $Cl + C_2H_6$ reaction mentioned earlier, which is contrary to the experimental observation of severe

depletion of products at certain scattering angles (figure 2). A correction function can be generated to apply to experimental data to remove any biases revealed by the MC simulations (denoted here as f_{sim}), but will not account for the majority of the under-detection of certain products we observe experimentally. The simulations do not, however, incorporate the possibility of secondary collisions of the nascent reaction products with the pulses of gas in the on-axis molecular beam. Despite the use of a skimmer in this beam, we speculate that such collisions are the cause of the observed depletion; products scattered in a direction that opposes the velocity of the CM (which lies vertically upward in our experiment) have lower lab frame speeds than those scattered in other directions, and thus spend longer in the vicinity of the on-axis molecular beam, making them more prone to secondary collisions. To test this hypothesis, we created a further correction function from our simulations that is based on the time the product Cl atoms spend from formation to detection, and are thus within the region of the on-axis molecular beam. We denote this time as t_{Cl}. The secondary collisions that are suggested to deplete reaction products from the probe laser volume can be modelled as a pseudo-first order process, with the molecular beam species in great excess over the reaction products. This suggests a dependence of collision probabilities that is exponential in t_{Cl} (scaled by the minimum value of this time, t_{Cl}^{min}, but we also considered a linear dependence. The full correction functions $f_{sim}\exp(t_{Cl} / t_{Cl}^{min})$ and $f_{sim}t_{Cl}$ for reaction of the slow CH_3 radical subset are shown in the lower panel of figure 3 for these two scenarios. The former scenario reproduces semi-quantitatively the correction factor derived from experimental comparison of dual- and crossed-beam data for the Cl + C_2H_6 reaction shown in figure 2, supporting our use of this experimental correction factor for other data. It should be noted that the angular coordinate system is reversed on going from the Cl + C_2H_6 reaction, to the CH_3 + HCl reaction, as in the former the abstraction product (HCl) is detected and in the latter the spectator product (Cl) is imaged.

4. Results and discussion

Figure 4 shows typical DC slice velocity map images obtained for the Cl($^2P_{3/2}$) products of the reaction of CH_3 and CD_3. The methyl radicals travel upwards from the bottom of the images and define the direction of the CM velocity vector. The bimodal collision energy distribution gives rise to mean CM velocities of 1425 (1460)

ms^{-1} and 1115 (1120) ms^{-1} for the reactions of the fast and slow CH_3 (CD_3) radicals with HCl respectively, and the maximum CM velocities resulting from the distributions of slow and fast CH_3 (CD_3) speeds can be calculated from the conservation of energy and linear momentum to be 1635 (1690) and 1245 (1300) ms^{-1} respectively. The CM velocity defines the centre of a Newton sphere of product speeds, so images consist of two overlaid Newton spheres of reaction products as depicted in panel c of figure 4, further broadened by the spread of CM speeds within the fast and slow CH_3 groups. In these images, the scattering angle for undetected methane is defined relative to the velocity vector of the reagent methyl radicals, and for Cl products, as noted earlier, we define the scattering angle with respect to the relative velocity vector of the HCl reagent; forwards (0^o) scattering of Cl atoms is therefore downwards in the velocity map image and backwards scatter (180^o) is upwards. The presence of the beam block, as described earlier, prevents complete observation of scattering below an angle of ~30^o.

The Cl images show the majority of products to have an angular distribution centred on a single point corresponding to the CM velocity for collisions of the slow methyl reagent. An initial analysis procedure therefore assumes this single centre to the image and is used for a first estimate of the form of the velocity distributions for all reaction products. In this analysis, the velocity distribution is obtained for scattering angles between 150 and 180 degrees where, as the Newton diagram in figure 4 shows, there is good separation between the speeds of products from fast and slow CH_3 reactions. The velocity distribution of the Cl atom products from the CH_3+HCl reaction fits well to a pair of Gaussian functions, as shown in figure 5; these functions are centred at 775 ± 10 ms^{-1}, with a width of 430 ± 30 ms^{-1}, and 1305 ms^{-1} ± 50 ms^{-1}, with a width of 420 ± 90 ms^{-1}, and can be assigned to reaction of the slow and fast methyl radicals, respectively, in accord with the energetic cut-offs in speed indicated in figure 5 for the two channels. From the integrated areas of the Gaussian functions, and the known branching between I* and I channels in CH_3I photodissociation at 266 nm, the relative reactivity of the lower to the higher collision energy channels is determined to be 1.4 ± 0.4 for the Cl products formed in the backwards scattered direction. It should be noted that this simplified analysis biases against fast products, but the effect of this bias is estimated to be less than the reported error in the branching ratio.

To accommodate the effect of two CM velocities in the Newton diagram and the velocity map images in a more sophisticated analysis, the extraction of angular scattering and speed distributions for both channels was carried out by a computational forwards simulation of the images, including contribution from both fast and slow channels using assumed, but adjustable forms of the speed distributions and the angular scattering. The contributions of the channels are initially weighted according to the branching ratio for the formation of fast and slow CH_3 (CD_3) in the photodissociation step, but then allow further variation to account for possible differences between the reactivity of the fast and slow methyl radicals. The product speed distributions are assumed to be Gaussian functions, with an initial guess for the centres and widths derived from the preliminary analysis described above. We assume identical angular scattering for the reaction of fast and slow methyl radicals, which is supported by the outcomes of previous, single-beam co-expansion experiments. These earlier experiments showed that, within experimental error, the differential cross sections for Cl and Cl* products were the same, and the latter products were argued to be favoured by reaction of the fastest CH_3 radicals while the former were produced by the reaction of both fast and slow CH_3 radicals [44,22]. A simulated image that best matches the experimental data is determined by manually varying the centres and widths of the velocity distributions, the angular scattering distribution and relative contribution of the fast and slow channels, and comparing with the experimental image by calculation of the residual differences between the two.

The best simulated images from the results of this procedure are displayed in figure 4. To constrain the number of parameters used to generate the simulated images, the angular scattering distribution was chosen to be a linear function of angle with a variable gradient, before application of the experimentally derived correction factor described in section 2. This choice necessarily limits the angular resolution of the experiment but is sufficient to reproduce the main features of the images. The Gaussian speed distributions obtained from this image analysis for the Cl products of the reaction of CH_3 with HCl are centred at 770 ms^{-1}, with a width of 450 ms^{-1}, for the slow methyl channel and at 990 ms^{-1}, with a width of 500 ms^{-1}, for the fast channel. The ratio for Cl products from the slow and fast CH_3 radicals is 3.2 : 1, and correction for the photolytic branching ratio gives a ratio of the reactivity of 1.5 : 1. Varying the

product speed parameters for the slow channel by ~25 ms^{-1}, the fast channel by ~50 ms^{-1} and the weighting of the channels by ~15% does not significantly alter the quality of the simulation. The best simulation of the product image of the reaction of CD_3 with HCl is obtained with Cl speed distributions described by Gaussians centred at 780 ms^{-1}, with width 490 ms^{-1} for the slow methyl channel and 1000 ms^{-1}, with width 550 ms^{-1}, for the fast channel. Changing the Gaussian centre speeds for the slow channel by ~25 ms^{-1} and the fast channel by ~100 ms^{-1} again does not significantly alter the agreement between simulation and experiment. The greater uncertainty in the speed distribution for products of the fast methyl radical reaction channel is a consequence of the lower signal levels in the experiments. The ratio of Cl products from reaction of slow and fast CD_3 radicals is ~11: 1, indicating a relative reactivity (corrected for the photolytic branching) of 2.5: 1 for the CD_3 + HCl reaction, but the low signal levels mean that the uncertainty in this value is high.

While the assumptions made in the simulation procedure, particularly the separability of the speed and angular distributions of products, and the angular scattering being independent of collision energy, result in satisfactory simulations of the experimental images, we cannot be certain that the outcomes of the analysis reported above provide a unique answer. We are limited by the number of parameters required to describe the speed and angular distributions for two overlapping sets of Newton spheres with displaced CM velocities, the loss of information in the forwards scattering direction for Cl atoms because of the presence of the beam block, likely depletion of products scattered in the downward direction in the lab, and low signal levels. We are thus unable to carry out more systematic fits of the images to basis functions describing the speed and angular scattering distributions. Deductions about the relative reactivity of the fast and slow CH_3 (CD_3) fragments rely on the quality of the simulations in the backwards scattered direction (the upper hemisphere of the images) and the assumption that the DCSs are the same for both collision energy regimes. By considering a line-of centres model for the CH_3 + HCl reaction, we might expect the DCS to become more strongly forwards scattered as the collision energy increases, thus the derived apparent enhancement in the reactivity of the slow CH_3 (CD_3) fragments is more likely to be over than under-estimated. For both sets of reagent speeds, however, the collision energy is well in excess of the barrier height, so this effect is anticipated to be small.

The DCSs and distribution of translational energy release, expressed as a fraction f_t of the total available energy, derived from the angular and speed distributions used for the image simulations for CH_3 + HCl and CD_3 + HCl are shown in figures 6 and 7 respectively. The f_t distributions for the fast and slow methyl reagent channels are similar, with comparable widths and $\langle f_t \rangle$=0.43 ± 0.05 for the fast channel and 0.47 ± 0.03 for the slow channel of the CH_3 + HCl reaction, with the balance of energy going into the internal motions of the undetected methane co-product. The mean f_t values quoted above assume uniform detection of products across the range of f_t values, however MC simulation outcomes shown in figure 3, suggest that the experiment biases against the detection of products with high f_t. Correction of our f_t distributions to account for this bias by dividing by the form of P(f_t) in figure 3 results in revised values of $\langle f_t \rangle$ = 0.48 and 0.50 for the reaction of fast and slow CH_3, respectively. The values for the reaction of CD_3 are comparable, being $\langle f_t \rangle$=0.43±0.08 for the fast channel and 0.46±0.03 for the slow channel (which are revised to 0.49 and 0.52 after application of MC-derived correction function). Thus the CH_4 (CD_3H) product is formed internally excited with approximately half of the available energy, consistent with an early barrier to reaction in this direction and coupling of the reaction coordinate to the bending modes of the methane [44]. The fractional kinetic energy release deduced in these experiments is lower than the values obtained previously using single-beam co-expansion experiments with PHOTOLOC and LM analysis which gave values of $\langle f_t \rangle$ = 0.61 and 0.64 respectively (the latter value has been corrected from our previously published value to allow for an improved analysis). The new f_t results reported here for both reactions exclude the most forward scattered products but this is unlikely to account for the discrepancies in $\langle f_t \rangle$ between methods. The differences are significant, but we note that a similar discrepancy between f_t distributions is observed for the HCl products of the Cl + C_2H_6 reaction: when studied in crossed-beam or dual-beam experiments, $\langle f_t \rangle \sim 0.62$ is measured, compared to $\langle f_t \rangle \sim 0.80$ derived from single-beam experiments [23]. The disagreement may therefore be a consequence of assumptions made in the analysis of data from the co-expansion experiments.

The DCSs for the CH_3 + HCl and CD_3 + HCl reactions are plotted as P(cos θ) which (is proportional to dσ/dcos θ) in figures 6 and 7 and are the same within experimental error. The data have been corrected for the bias against scattering downwards in the lab frame, against the CM velocity, using the angular correction function plotted in figure 2, and the resultant DCSs peak in the forwards direction. The uncertainties in the forward scattered amplitude will be large because of the form of the angular correction factor employed, but the outcomes are consistent with a stripping mechanism for a reaction at high collision energy. Comparison with previous single-beam co-expansion experiments analysed using the PHOTOLOC and LM methods (the latter subject to a refined analysis from our previously published results [44]) show reasonable general agreement: all DCSs are derived to peak in the forwards scattered direction.

Both a preliminary analysis of the backwards scattered region (the upper hemisphere) of the image (figure 5), and simulations of the full image indicate (figure 4) that the slow CH_3 fragments account for ~76% of the observed $Cl(^2P_{3/2})$ reaction products, suggesting an enhanced reactivity compared to the fast methyl fragments by a factor of ~1.5 (when the photolytic branching of CH_3I to slow and fast CH_3 radicals is allowed for). Previous co-expansion experiments have shown that there is a 15% branching into the non-adiabatic $Cl^*(^2P_{1/2})$ channel, however, and there is evidence that this non-adiabatic pathway is favoured by the reaction of the faster subset of methyl fragments [22,42]. The photolytic production of this fast subset from the photolysis of CH_3I at 266 nm occurs with a branching ratio of 0.32. In the limit that non-adiabatic reaction to Cl* occurs solely via the reaction of the faster methyl reagents, an assumption of equal total reaction probabilities with HCl for slow and fast CH_3 radicals would predict that the former should account for 80% of the ground-state Cl products. A second limiting case model can be postulated which assumes no dependence of the probability of the non-adiabatic reaction on the speed of the CH_3 fragments: an equal total reaction probability for fast and slow CH_3 radicals would result then in 68% of the observed Cl atoms coming from the slow CH_3 radicals. This fraction is dictated solely by the branching into slow and fast CH_3 channels in the photoinitiation step. These two simplified models can also be tested using the CD_3+HCl data. The 266 nm photolysis of CD_3I produces 81% slow CD_3 and 19% fast CD_3, and non-adiabatic dynamics of the reaction with HCl to form Cl* now

accounts for 20% of the products. Within the approximations of the first model, the predicted fraction of Cl atoms from slow CD_3 reagents is 100%; whereas for the second limiting model, this fraction is 81%. Experimentally the slow methyl fragments account for ~76% of the observed Cl products in the CH_3+HCl reaction and ~92% in the CD_3+HCl reaction and these values are intermediate between the limiting case models outlined above, but are more consistent with the first We therefore conclude that the total reaction cross-section for the slow and fast CH_3 (or CD_3) reaction with HCl are similar, and the greater apparent branching to Cl atom products for the slow subset of CH_3 (or CD_3) reagents is largely a consequence of the faster radicals being more likely to undergo non-adiabatic reaction to form Cl*.

As noted previously [44], it is unlikely that non-adiabatic reaction proceeds only via reaction of the fast channel, but instead flux from both the lower and higher collision energy regimes will couple to the excited state potential energy surface (PES) correlating to CH_4+Cl* products. The non-Born-Oppenheimer couplings are mediated by the nuclear kinetic energy, and become more significant for higher collision energies. Our data from this and prior studies, suggest that at the high collision energies for reactions of both the fast and slow subsets of CH_3 (CD_3) radicals, the probability of formation of Cl* atoms is greater for the fast CH_3 (CD_3) radicals: we can now estimate that the reactivity of the fast methyl fragments to give Cl* is about 7 times greater than for the slow methyl fragments for both the CH_3+HCl and CD_3+HCl reactions. This estimate accounts for the difference in branching into the fast and slow methyl reagents in the photoinitiation step, but assumes the total overall reactivity of the fast and slow methyl radicals with HCl is equal, despite differences in the vibrational content of the methyl radicals (see section 2), and that the DCSs are identical. This latter assumption means that the value for relative reactivity to form Cl* is likely to be an upper estimate. The analysis would be made more robust by velocity map imaging of the scattering of Cl* reaction products. Unfortunately, low signal-to-noise levels mean that these non-adiabatic products have not yet been observed in our dual-beam VMI experiments. Further investigation of the reactivity of the fast and slow methyl fragments via the electronically non-adiabatic channel therefore remains a future objective.

5. Conclusions

The application of dual beam and velocity map imaging methodologies to the study of the dynamics of reactions of CH_3 and CD_3 radicals with HCl has enabled separation of the contributions to reactions of two different speed groups of methyl radicals. These two speed groups arise from the 266-nm photodissociation of CH_3I or CD_3I to generate the methyl radical reagents. The relative reactivities of the slower radicals for the production of $Cl(^2P_{3/2})$ products are greater than for the faster radicals by a factor of ~1.5 for the CH_3 + HCl reaction and ~2.5 for the CD_3 + HCl reaction. With allowance for competition to form Cl* (not probed here) by non-adiabatic dynamics, the overall reactivities of the faster and slower methyl radicals with HCl are, however, deduced to be very similar. The mean fractions of the total available energy becoming product translational energy, $\langle f_t \rangle$ = 0.48± 0.05 and 0.50 ± 0.03 respectively, for the faster and slower sets of CH_3 in the case of the CH_3 + HCl reaction are the same within the experimental uncertainties.

The implementation of the dual beam method, although in principle allowing direct velocity map imaging of the scattering in the centre-of-mass frame, introduces certain experimental difficulties that have required Monte Carlo simulation methods to understand, and necessitate application of empirical corrections factors to the raw experimental data. In particular, the reaction products with low laboratory frame speeds spend longer in the vicinity of a skimmed, pulsed molecular beam prior to laser detection than do the faster moving products. This makes these slower products more vulnerable to secondary collisions with particles in the molecular beam that scatter them away from the probe laser. In the case of the CH_3 (CD_3) + HCl reaction, the forward scattered Cl products (with scattering angle defined with respect to the direction of the HCl component of the relative velocity of the reagents) have velocities in the CM frame that oppose the velocity of the CM of the system. They thus acquire low laboratory fame speeds and spend a few microseconds longer than backward scattered products before reaching the probe laser volume. A scattering angle dependent function can be applied to the raw data to correct for this under-detection, and is derived either from the Monte Carlo simulations of the experiment, or, as in the current study, from use of a calibration reaction for which the differential cross section is well established by crossed molecular beam experiments. The Cl +

C_2H_6 reaction proved to serve well for this calibration procedure. Following application of the correction function, the angular scattering distribution is in reasonable agreement with results from prior experiments making use of photoinitiation of reaction in a single molecular beam expansion. Previous studies by Kitsopoulos and coworkers using the dual beam method in a different apparatus did not require the type of correction to the angular scattering distribution reported here [31,33].

Image analysis is further complicated by the bimodal speed distribution of the CH_3 (or CD_3) radicals from the UV photolysis of methyl iodide. The distributions of collision energies for the reactions of CH_3 or CD_3 with HCl are thus also bimodal, and the faster and slower groups of methyl radicals give rise to two distinct but overlapping Newton diagrams for the scattering of the reaction products, centred about two different positions (and thus speeds) in the velocity mapped images. Direct image inversion to obtain speed and angular scattering distributions was thus not possible, and to deconvolute the overlapping scattering distributions, a forward simulation of the images was employed based on trial product speed and angular scattering distributions. Nevertheless, the analysis procedure allowed estimates of the distributions of f_t and the differential cross sections for the electronically adiabatic channels of these benchmark radical reactions.

6. Acknowledgements

We are grateful to EPSRC for financial support via the EP/G00224X Programme Grant and to the University of Bristol for a Postgraduate Scholarship (R.A.R.). S.J.G. thanks the Leverhulme Trust for an Early Career Research Fellowship and A.J.O.E. is grateful to the Royal Society and the Wolfson Foundation for a Research Merit Award. We thank Dr C.S. Huang and Prof. A.G. Suits (Wayne State University) for providing us with the crossed-beam data for the Cl + ethane reaction.

Figure captions

Figure 1: A schematic diagram of the experimental set-up. R, L_1, L_2, and G are the repeller, two electrostatic lenses and grounded electrode used for velocity mapping; MCPs are microchannel plates, P47 is a fast decay phosphor screen and PMT is a photomultiplier tube. The valve set-up used for the dual beam experiments is shown in an expanded view on the left.

Figure 2: An HCl(v=0,J=1) product image from the Cl + C_2H_6 reaction obtained using the dual beam image technique at a collision energy of 5.4 kcal mol^{-1} is shown on the left. The centre-of-mass velocity is indicated by the u_{CM} vector, and product HCl scattering in the centre-of-mass frame is illustrated by one u_{HCl} vector at a scattering angle θ. The outer dotted circle shows the limit on the HCl speed imposed by the energetics and kinematics of the reaction. The angular distribution of the HCl products derived from the image is shown on the right (grey line) and is compared to the crossed beam results of Suits and coworkers at a collision energy of 6.7 kcal mol^{-1} (black line) [3]. The experimental angular scattering correction factor (dashed line) is derived by dividing the crossed molecular beam DCS by that obtained in the dual-beam experiment.

Figure 3: Fractional translational energy release (f_t) (upper panel), angular scattering distributions (middle panel) and angular correction factors (lower panel) produced using the Monte Carlo simulation program. The panels show the derived f_t and DCS distributions for reaction of the fast (solid line) and slow (dashed line) methyl radicals, for sampling from uniform f_t and angular distributions (blue lines in the top and middle panels). The angular correction factors in the lower panel are derived by multiplying the bias in the experiment, deduced from data in the middle panel, by either t_{Cl} (solid line) or $\exp(t_{Cl} / t_{Cl}^{min})$ (dash-dotted line); see the main text for definitions and further details.

Figure 4: Cl($^2P_{3/2}$) product images from the (a) CH_3+HCl and b) CD_3+HCl reactions and (c) Newton diagrams showing the velocity vectors of the centres of mass (u_{CM}) for reactions of slow (blue) and fast (red) CH_3 radicals, and representative centre-of-

mass frame velocity vectors (u_{Cl}) for the formation of Cl products, with the same colour coding. The images are divided to show experimental (left) and simulated (right) data, with simulations carried out using the procedure described in the text.

Figure 5: Velocity distribution derived from the CH_3+HCl reaction by analysis of the backwards scattered direction (180 to 150^o) of the velocity mapped images. The simplified analysis shown makes the approximation that the image centre for all scattering events is that for the reactions of slow methyl radicals (see text and figure 4). The experimental data (open circles) fit well to two Gaussian functions (grey lines) with the black line showing the total fit. The arrows mark the maximum speeds energetically available to Cl($^2P_{3/2}$) products from the reactions of fast and slow methyl radicals. The limit for the reaction of fast methyl radicals marked incorporates the difference in CM velocities of the fast and slow methyl radical reactions.

Figure 6: Angular scattering and fractional kinetic energy release (f_t) distributions which produce the simulated Cl atoms image shown in figure 4 for the reaction of CH_3 with HCl. The differential cross section (upper panel) has been corrected by an angle-dependent factor described in the main text. The experimental data (blue line) are compared to the PHOTOLOC (black line) [44] and LM (red line) analyses of single-beam co-expansion results. The error bars in the LM analysis were estimated from the precision of fits to replicate measurements and variations in the fit outcomes with the choice of basis functions, and encompass the range of values obtained. The lower panel shows the reaction product f_t distributions for reaction of the faster (solid line) and slower (dashed line) methyl radicals with HCl. The distributions are derived from product speed distributions used in the simulations in figure 4 and the error bars on the f_t distributions are determined from the uncertainty in the centres and widths of the Gaussian speed distributions

Figure 7: Angular scattering and fractional translational energy release distributions for the products of the CD_3 + HCl reaction. All further details are the same as for the caption to figure 6.

References

[1] R.D. Levine, Molecular Reaction Dynamics, (Cambridge University Press, Cambridge, 2005).
[2] W. Li, C.S. Huang, M. Patel, D. Wilson, A.G. Suits, J. Chem. Phys. **124**, 011102 (2006).
[3] C.S. Huang, W. Li, A.G. Suits, J. Chem. Phys. **125**, 133107 (2006).
[4] J. Zhou, B. Zhang, J.J. Lin, K. Liu, Mol. Phys. **103**, 1757 (2005).
[5] J. Zhou, J.J. Lin, W. Shiu, S.-C. Pu, K. Liu, J. Chem. Phys. **119**, 2538 (2003).
[6] H. Kawamata, S. Tauro, K. Liu, Phys. Chem.Chem. Phys. **10**, 4378 (2008).
[7] Y.T. Wu and K. Liu, J. Chem. Phys. **129**, 154302 (2008).
[8] S. Yan, Y.T. Wu, K. Liu, Phys. Chem. Chem. Phys. **9**, 250 (2007).
[9] S. Yan, Y.T. Wu, B.L. Zhang. X.F. Yue, K.Liu, Science **316**,1723 (2007).
[10] B. Zhang and K. Liu, J. Chem. Phys. **122**, 101102 (2005).
[11] W. Shiu, J.J. Lin, K. Liu, Phys. Rev. Lett. **92**, 103201 (2004).
[12] J.J. Lin, J.G. Zhou, W. Shiu, K. Liu, Science **300**, 966 (2003).
[13] J. Zhou, J.J. Lin, W. Shiu, K. Liu, J. Chem. Phys. **119**, 4997 (2003)
[14] W. Shiu, J.J. Lin, K. Liu, M. Wu, D.H. Parker, J. Chem. Phys. **120**, 117 (2004)
[15] J. Zhou, W. Shiu, J.J. Lin, K. Liu, J. Chem. Phys. **120**, 5863 (2004).
[16] J. Zhou, J.J. Lin, W. Shiu, K. Liu, Phys. Chem. Chem. Phys. **8**, 3000 (2006).
[17] B. Zhang, K. Liu, J. Phys. Chem. A **109**, 6791 (2005).
[18] W.Q. Zhang, G.R. Wu, H.L. Pan, Q. Shuai, B. Jiang, D.X. Dai, X. Yang, J. Phys. Chem. A **113**, 4652 (2009).
[19] N.E. Shafer, A.J. Orr-Ewing, W.R. Simpson, H. Xu, R.N. Zare, Chem. Phys. Lett. **212**, 155 (1993).
[20] F.J. Aoiz, M. Brouard, P.A. Enriquez, R. Sayos, J. Chem. Soc. Faraday Trans. **89**, 1427 (1993).
[21] S.A. Kandel, T.P. Rakitzis, T. Lev-On, R.N. Zare, J. Chem. Phys. **105**, 7550 (1996).
[22] B. Retail, S.J. Greaves, J.K. Pearce, R.A. Rose, A.J. Orr-Ewing, Phys. Chem. Chem. Phys. **9**, 3261 (2007).
[23] M.J. Bass, M. Brouard, C. Vallance, T.N. Kitsopoulos, P.C. Samartzis, R.L. Toomes, J. Chem. Phys. **119**, 7168 (2003).
[24] M.J. Bass, M. Brouard, C. Vallance, T.N. Kitsopoulos, P.C. Samartzis, R.L. Toomes, J. Chem. Phys. **121**, 7175 (2004).
[25] M.J. Bass, M. Brouard, R. Cireasa, A.P. Clark, C. Vallance, J. Chem. Phys. **123**, 094301 (2005).
[26] L. Schnieder, K. Seekamp-Rahn, F. Liedeker, H. Steuwe, K.H. Welge, Faraday Discuss. Chem. Soc. **91**, 259 (1991).
[27] X. Liu, J.J. Lin, S. Harich, G.C. Schatz, X.Yang, Science **289**, 1536 (2000).
[28] T.N. Kitsopoulos, M.A. Buntine, D.P. Baldwin, R.N. Zare, D.W. Chandler, Science **260**, 1605 (1993).
[29] X. Liu, R.L. Gross, A.G. Suits, J. Chem. Phys. **116**, 53141 (2002).
[30] G. Wu, W. Zhang, H. Pan, Q. Shuai, B. Jiang, D. Dai, X. Yang, Rev. Sci. Instrum. **79**, 094104 (2008).
[31] R.L. Toomes, T.N. Kitsopoulos, Phys. Chem. Chem. Phys. **5**, 2481 (2003).
[32] R.L. Toomes, A.J. van den Brom, T.N. Kitsopoulos, C. Murray, A.J. Orr-Ewing, J. Phys. Chem. A **108**, 7909 (2004).
[33] C. Murray, A.J. Orr-Ewing, R.L. Toomes, T.N. Kitsopoulos, J. Chem. Phys. **120**, 2230 (2004).
[34] W.R. Simpson, A.J. Orr-Ewing, R.N. Zare, Chem. Phys. Lett. **212**, 163 (1993).
[35] C. Murray and A.J. Orr-Ewing, Int. Rev. Phys. Chem. **23**, 435 (2004) and references therein.
[36] W.R. Simpson, T. P. Rakitzis, S.A. Kandel, A.J. Orr-Ewing, R.N. Zare, J. Chem. Phys. **103**, 7313 (1995).
[37] Z.H. Kim, H.A. Bechtel, R.N. Zare, J. Am. Chem. Soc. **123**,12714 (2001).
[38] H.A. Bechtel, Z.H. Kim, J.P. Camden, R.N. Zare, J. Chem. Phys. **120**, 791 (2004).
[39] S. Yoon, R.J. Holiday, F.F. Crim, J. Chem. Phys. **119**, 4755 (2003).
[40] B. Retail, J.K. Pearce, C. Murray, A.J. Orr-Ewing, J. Chem. Phys. **122**, 101101 (2005).
[41] D. Townsend, M.P. Minitti, A.G. Suits, Rev. Sci. Instrum. **74**, 2530 (2003).
[42] B. Retail, R.A. Rose, S.J. Greaves, J.K. Pearce, A.J. Orr-Ewing, Phys. Chem. Chem. Phys. **10**, 1675 (2008).
[43] J.K. Pearce, B. Retail, S.J. Greaves, R.A. Rose, A.J. Orr-Ewing, J. Phys. Chem. A **111**, 13296 (2007).
[44] B. Retail, J.K. Pearce, S.J. Greaves, R.A. Rose, A.J. Orr-Ewing, J. Chem. Phys. **128**, 184303 (2008).

[45] J.K. Pearce, Ph.D. Thesis, University of Bristol (2007).
[46] A.T.J.B Eppink and D.H. Parker, J. Chem. Phys. **110**, 832 (1999).
[47] G.S. Li and H.J. Hwang, J. Chem. Phys. **124**, 244306 (2006).

Figure 1

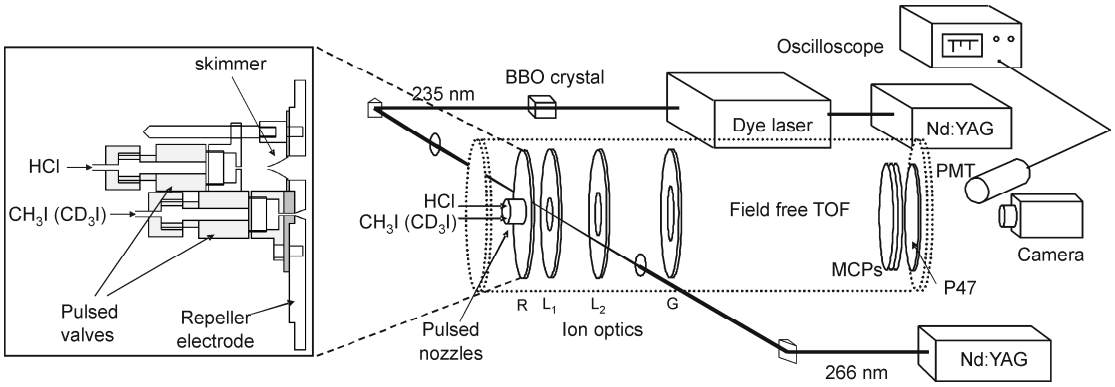
skimmer
HCl
CH_3I (CD_3I)
Pulsed valves
Repeller electrode
235 nm
BBO crystal
HCl
CH_3I (CD_3I)
Pulsed nozzles
R
L_1
L_2
G
Ion optics
Dye laser
Oscilloscope
Nd:YAG
PMT
Field free TOF
Camera
MCPs
P47
266 nm
Nd:YAG

Figure 2

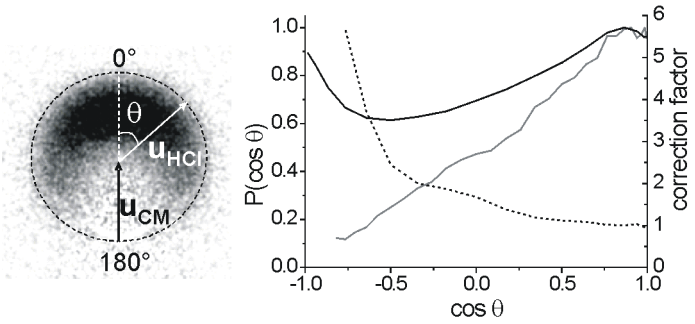
0°
θ
u_HCl
u_CM
180°
P(cos θ)
correction factor
cos θ
1.0
0.8
0.6
0.4
0.2
0.0
-1.0
-0.5
0.0
0.5
1.0
6
5
4
3
2
1
0

Figure 3

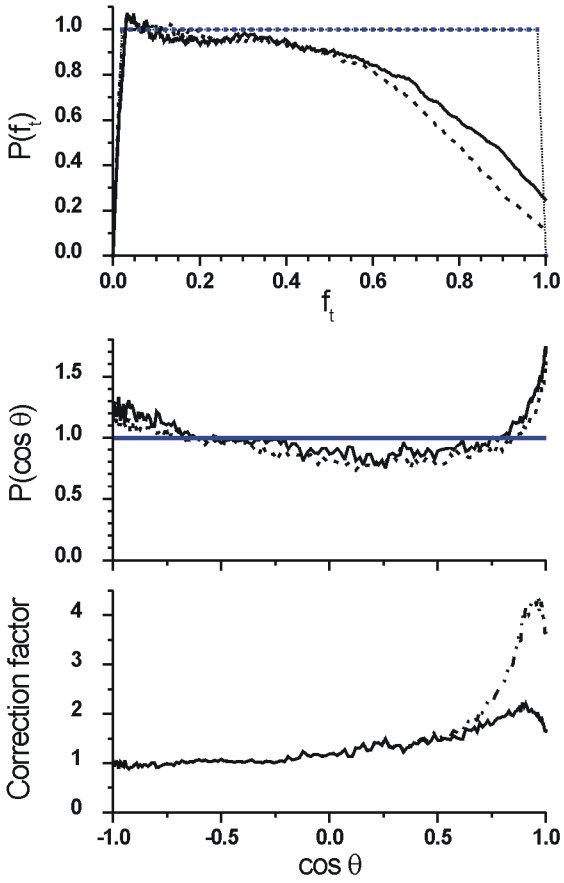

Figure 4

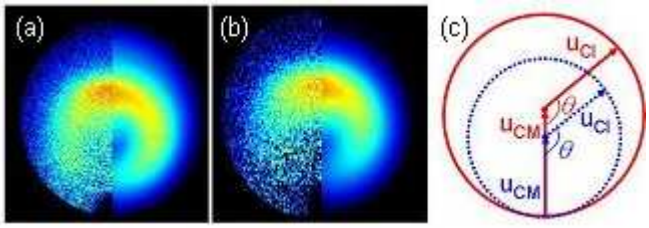

Figure 5

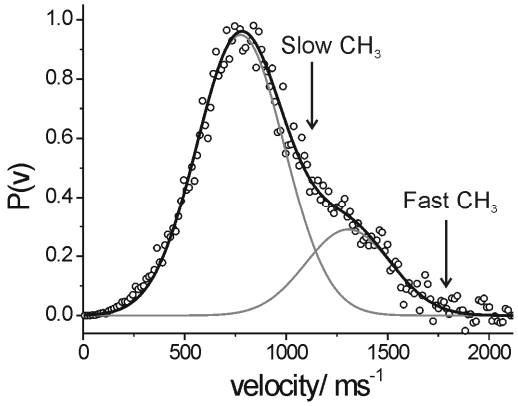
1.0
0.8
0.6
0.4
0.2
0.0
P(v)
Slow CH3
Fast CH3
0
500
1000
1500
2000
velocity/ ms-1

Figure 6

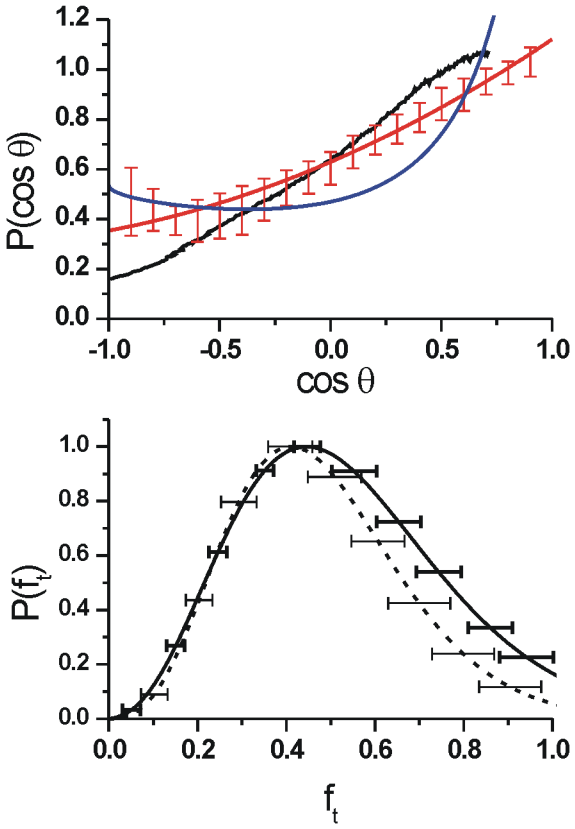

Figure 7